

High-Throughput Microfluidics Platform for Intracellular Delivery and Sampling of Biomolecules from Live Cells

Cesar A. Patino, Prithvijit Mukherjee, Eric J. Berns, Elamar Hakim Mouly, Liliana Stan, Milan Mrksich, and Horacio D. Espinosa*



Cite This: <https://doi.org/10.1021/acsnano.2c00698>



Read Online

ACCESS |



Metrics & More



Article Recommendations

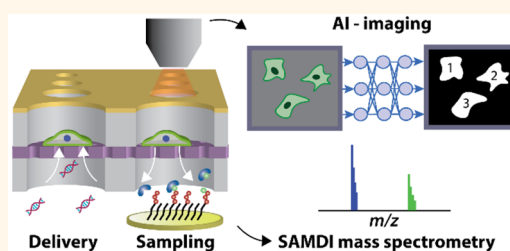


Supporting Information

ABSTRACT: Nondestructive cell membrane permeabilization systems enable the intracellular delivery of exogenous biomolecules for cell engineering tasks as well as the temporal sampling of cytosolic contents from live cells for the analysis of dynamic processes. Here, we report a microwell array format live-cell analysis device (LCAD) that can perform localized-electroporation induced membrane permeabilization, for cellular delivery or sampling, and directly interfaces with surface-based biosensors for analyzing the extracted contents. We demonstrate the capabilities of the LCAD via an automated high-throughput workflow for multimodal analysis

of live-cell dynamics, consisting of quantitative measurements of enzyme activity using self-assembled monolayers for MALDI mass spectrometry (SAMDI) and deep-learning enhanced imaging and analysis. By combining a fabrication protocol that enables robust assembly and operation of multilayer devices with embedded gold electrodes and an automated imaging workflow, we successfully deliver functional molecules (plasmid and siRNA) into live cells at multiple time-points and track their effect on gene expression and cell morphology *temporally*. Furthermore, we report sampling performance enhancements, achieving saturation levels of protein tyrosine phosphatase activity measured from as few as 60 cells, and demonstrate control over the amount of sampled contents by optimization of electroporation parameters using a lumped model. Lastly, we investigate the implications of cell morphology on electroporation-induced sampling of fluorescent molecules using a deep-learning enhanced image analysis workflow.

KEYWORDS: cell sampling, deep learning, electroporation, enzymatic activity, intracellular delivery, microfluidics



Recent advances in the fields of microfluidics and biosensors have led to transformative capabilities for cell analysis and manipulation with significant implications in cell engineering and fundamental cell biology research.¹ Specifically, mechanisms to open reversible pores in the cell membrane were developed to enable the delivery of exogenous materials into live cells, targeting a broad range of applications from gene editing and cell-line generation to stem-cell reprogramming.^{2–6} Physical membrane-poration methods, i.e., electroporation^{7,8} and mechanoporation,^{9–11} provide enhanced dosage control and uniformity across various cell types compared to lipid-vesicle carriers and viral vectors.² Furthermore, improvements to both dosage control and cell health are possible through the miniaturization of these technologies down to the micro- and nanoscales.^{4,12,13} A nanoscale method known as localized electroporation, utilizes geometric confinements, i.e., nanochannels, to localize an applied electric field to a small area fraction on the cell membrane that results in the formation of pores when the electric potential across the cell membrane (transmembrane

potential or TMP) exceeds a threshold value (~ 0.5 V).^{4,14–17} The localized electric field enables the formation of pores at low applied voltages, compared to bulk electroporation systems, and facilitates electrophoretic transport of charged molecules into the cytoplasm.^{13,16–18} Consequently, the amount of delivered material in these systems can be tuned by adjusting the electrical stimulation parameters such as applied voltage and pulse duration while maintaining high cell viability necessary for repeated stimulations. Molecules of various sizes, ranging from small hairpin-molecular beacons to large plasmids and CRISPR/Cas9 complexes, have been

Received: January 20, 2022

Accepted: April 26, 2022

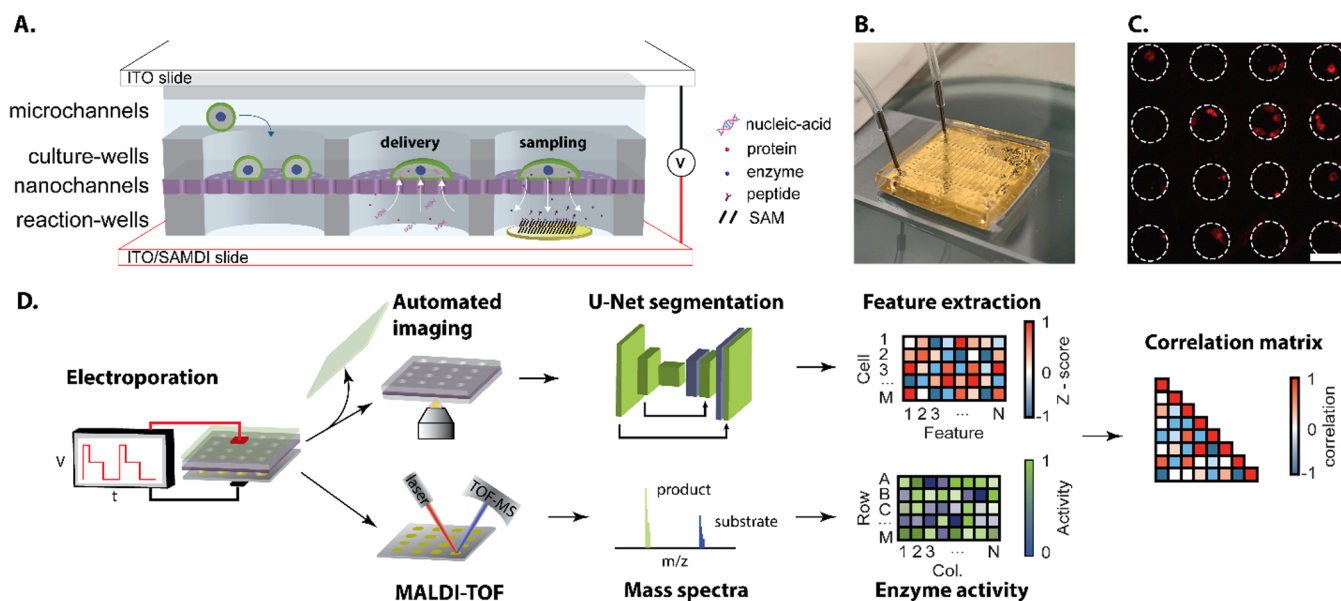


Figure 1. LCAD design and high-throughput analysis workflow. (A) Schematic of multilayer architecture enables three modes of operation: cell seeding, delivery, and sampling. (B) Photograph of assembled LCAD device. (C) Fluorescence micrograph of Td-Tomato expressing MDA-MB231 cells cultured in the PDMS culture wells. Scale bar = 100 μm . (D) Multimodal analysis workflow consisting of automated imaging of LCAD culture wells followed by deep-learning cell detection and feature extraction (top) and high-throughput enzyme activity measurements of SAMDI slide with a MALDI-TOF mass spectrometer (bottom).

delivered into a wide diversity of cell types utilizing localized electroporation.^{4,19–21}

The reverse process, cytosolic extraction (sampling), is also possible with membrane poration techniques. Measuring biomarkers sampled from live cells provides researchers with the ability to study dynamic cellular processes like differentiation and signal transduction as they unfold, whereas measurements obtained from cell lysates only reveal a snapshot of the process.²² Devices designed to sample intracellular contents include nanopipettes,²³ nanotweezers,²⁴ fluid-AFM probes,²⁵ nanochannels,²⁶ and nanostraws.^{27,28} Probe-based configurations typically penetrate the cell membrane and retrieve sampled materials via electrowetting,²³ dielectrophoresis,²⁴ or pressure-driven aspiration.²⁵ Nanochannel membrane systems utilize localized electroporation to permeate the cell membrane and extract cytosolic materials from populations of cells. Although probe-based systems extract samples from single cells, an essential feature to study cell heterogeneity, the workflow is serial, which limits throughput, and the amount sampled is very small, placing major resolution demands on bioassays. Conversely, nanochannel systems can withdraw cytosolic samples from multiple cells in parallel, thereby improving throughput. However, using these systems, detection of sampled material from single cells remains challenging, and previous demonstrations have sampled from cell populations to exceed the limit of detection of assays such as ELISA and mRNA-sequencing.^{18,27,28} Thus, there is scope to improve the performance of nanochannel systems for sampling from single cells at high throughput.

Existing tools to open reversible pores in cells are widely used by researchers to deliver or extract materials across the cell membrane with precision and consistency. However, most designs are optimized to perform either delivery or sampling operations, not both, and some systems lack throughput to process and analyze large numbers of cells. Furthermore, existing sampling systems require the use of fluid handling

steps to retrieve and transport-sampled materials for downstream detection, which leads to material losses and dilution of analytes. In our recent work, we integrated the delivery and sampling functionalities in a single multilayer microfluidic chip, the live cell analysis device (LCAD), that utilizes localized electroporation to create pores in the cell membrane of cells seeded in an array of microwells.²⁶ The modular design of the LCAD enables a direct chip-to-sensor interface to avoid fluid handling steps and prevent losses of sampled material. We interfaced the LCAD with a sensitive label-free biosensors using self-assembled monolayers for MALDI mass spectrometry²⁹ to sample and quantify enzymatic activity from live cells at various time points.²⁶ Here, we report a fabrication protocol that enables robust assembly and operation of multilayer devices containing embedded gold electrodes and demonstrate a high-throughput analysis workflow that combines automated imaging with deep-learning-enhanced computer vision algorithms to extract information from live-cells following delivery and sampling experiments. Specifically, we perform a multi-time-point delivery study of functional plasmid and siRNA molecules, characterize the sampling performance with SAMDI as well as live-cell imaging, and investigate the role of cell morphology on the efficiency of sampling.

RESULTS AND DISCUSSION

Device Design. The LCAD is a multilayer microfluidic chip designed to nondestructively electroporate cells seeded in a microwell array format and to enable high-throughput experiments that involve the delivery or sampling of molecular cargoes. The device architecture (Figure 1A,B) consists of a PDMS microfluidic channel layer used for cell seeding and introduction of media and reagents, an array of through-hole PDMS culture wells ($n = 400$ wells) used to isolate small populations of cells (Figure 1C), a nanochannel polycarbonate (PC) membrane employed to confine the electric field during pulse application, and a PDMS reaction-well layer used to load

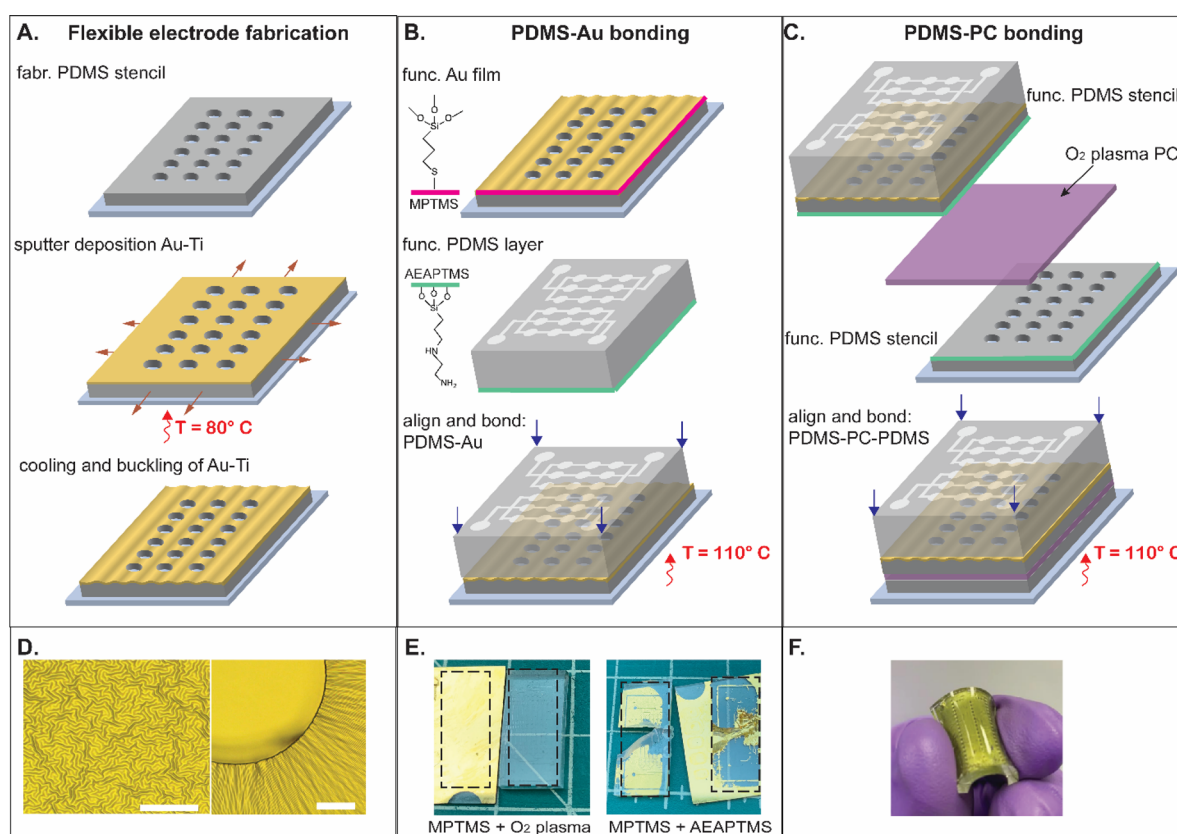


Figure 2. Fabrication and assembly of LCAD. (A) Schematic of steps used to fabricate a flexible metal layer on the PDMS culture wells. (B) Schematic of steps to bond the Au-coated culture wells to the PDMS microchannels. (C) Schematic of the assembly of the PC nanochannel membrane between the PDMS stencil layers. (D) Micrographs of the gold layer after electrode fabrication process (scale bars = 75 μm). (E) Images of PDMS block and Au-coated glass slide after peel test: (left) MPTMS-functionalized Au surface bonded to O₂ plasma activated PDMS and (right) MPTMS-functionalized Au surface bonded to AEAPTMS-functionalized PDMS. (F) Image of LCAD device after fabrication and assembly. Bending of the device is shown to illustrate flexible electrode fabrication.

delivery reagents and isolate sampled molecules. A modular interface enables connection of the LCAD to external equipment in order to achieve the three experimental functions (cell seeding, delivery, or sampling) independently.

For cell seeding and fluid handling operations, the inlet and outlet ports were connected to a flow-rate-programmable syringe pump via microbore tubing. To achieve efficient cell capture in the cell-culture microwells, we modeled the fluid flow in the LCAD microfluidic network using computational fluid dynamics (CFD) software (see the [Methods](#) for details and [Figure S1A,B](#)) and determined the optimal capture flow rate ($Q = 0.4 \mu\text{L}/\text{min}$). We experimentally tested the cell seeding procedure with the flow rate obtained from the CFD simulations and achieved efficient cell capture for wells of various sizes ([Figure S1C](#)). Accordingly, the cell population can be tailored by selecting a well of appropriate size and by optimizing experimental parameters such as cell density and seeding duration. After seeding cells in the culture wells, we clamped the LCAD between two conductive indium tin oxide slides (ITO), connected it to a programmable function generator, and applied electrical pulses to permeate the cells, enabling molecular transport across the cell membrane. The pulse shape (square, bilevel, or exponential decay) and voltage parameters (voltage amplitude, frequency, pulse duration, and number of pulses) were adjusted using a graphic user interface and optimized for each cell type and function (sampling or delivery).

The LCAD electroporation performance depends on the pulse parameters and the device design. In the LCAD, the nanochannel membrane is used to localize the electric field to a small area fraction of the cell membrane; therefore, the membrane porosity and pore diameter are relevant design parameters that affect the localized electroporation mechanism. Consequently, we implemented a lumped-circuit model to guide in the selection of the nanochannel membrane geometry and determine the applied voltage necessary to achieve the required transmembrane potential (TMP $\sim 0.5 \text{ V}$) to induce pore formation (see the [Supporting Information](#) for a detailed description of the lumped model analysis including Tables S1 and S2 and [Figure S2](#)). Our results indicate that the TMP decreases with increasing porosity for any given applied voltage and that the TMP increases exponentially with increasing cell confluency ([Figure S2B](#)). Therefore, low-porosity membranes result in a stronger localized electric field that is advantageous for electrophoretic transport processes such as delivery of charged molecules. Conversely, high-porosity membranes require higher applied voltages to achieve a threshold TMP but enable higher molecular transport through the nanochannels, which is an advantage for sampling applications. To enhance the electroporation performance of high-porosity membranes required for sampling, we modeled the LCAD with an additional gold electrode layer and found that this addition increases the predicted TMP of high porosity ($2 \times 10^8 \text{ pores cm}^{-2}$) membranes to similar magnitudes to that of the low

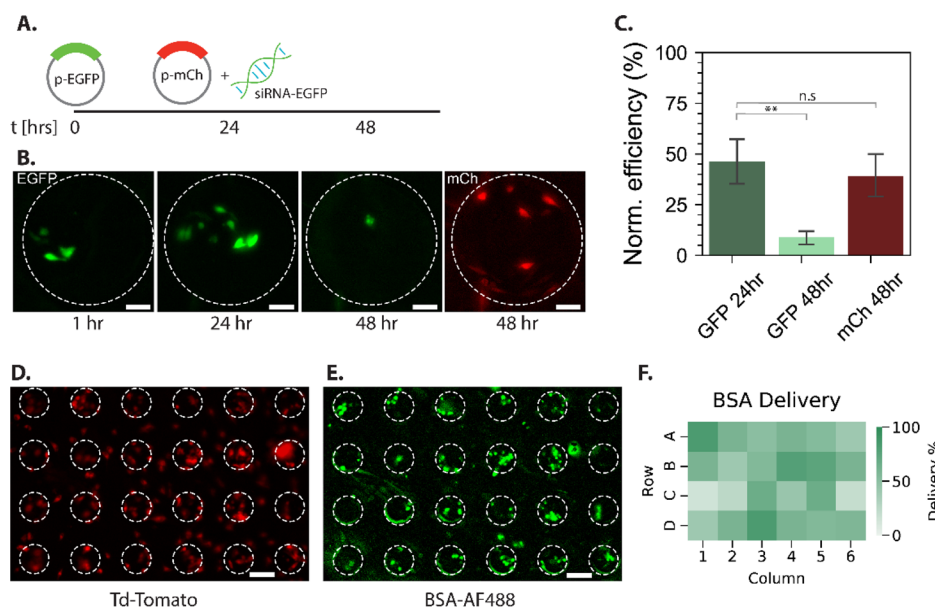


Figure 3. Multitime-point delivery and characterization of delivery uniformity. (A) Timeline of sequential delivery of EGFP plasmid and codelivery of EGFP-siRNA and mCherry plasmid. (B) Fluorescent micrographs obtained at different time-points for the same microwell. Scale bars = 50 μm . (C) Bar plot of plasmid expression max-min normalized by number of EGFP-expressing cells 24 h postdelivery. Standard error of mean bars ($N = 11$ wells). p -values used to determine statistical significance (n.s.: p -value > 0.05, **: $0.001 < p$ -value < 0.01). (D) Fluorescent micrographs of Td-Tomato expressing MDA-MB231 cells seeded in culture wells following delivery of (E) AF488-tagged BSA protein. Scale bars = 100 μm . (F) Heatmap of BSA delivery efficiency across the array.

porosity (2×10^7 pores cm^{-2}) membrane (see Figure S2C). As a result, we utilized the high porosity membrane with the embedded electrode configuration in subsequent experiments.

Device Fabrication and Assembly. The LCAD design consists of multiple thin layers comprised of different materials (PDMS, gold, and polycarbonate) that must be precisely aligned and robustly bonded together in order for the device to meet all of its design functions. To accomplish this, we employed a workflow consisting of three main steps: PDMS through-hole and flexible gold electrode fabrication (Figure 2A), bonding of gold electrode to PDMS microchannels (Figure 2B), and bonding of polycarbonate substrate to the two PDMS microwell layers (Figure 2C). We fabricated the PDMS microchannels using traditional soft lithography techniques. The fabrication of the through-hole layers required additional processing to increase yield. To this end, we implemented a surface chemistry technique that selectively polymerizes the PDMS by application of chelating amino-silanes on a transfer substrate.³⁰ This additional step resulted in PDMS through-holes in most of the wells ($\sim 98\%$) compared to controls without the functionalization steps ($\sim 50\%$). Next, we coated one PDMS stencil layer (culture wells) with gold to provide enhanced conductivity and uniform electric field conditions across the device as predicted from the lumped model (see Figure S2C). To prevent formation of cracks during assembly and device operation, we heated the PDMS substrate during the sputter deposition to induce buckling upon cooling of the thin metal film.^{31,32} The wavy surface (Figure 2D) resulted in increased flexibility of the metal film allowing it to withstand large strains without cracking.³³ To bond the Au-coated PDMS culture wells to the PDMS microfluidic channel layer, we functionalized the Au surface with a thiol-terminated silane, mercaptopropyltrimethoxysilane (MPTMS), and coated the surface of the PDMS with a double-amine silane, aminoethylaminopropyl-trimethox-

ysilane (AEAPTMS), to improve the bonding strength. We performed a peel test to compare the Au-PDMS bond strength of two conditions (Figure 2E): an oxygen-plasma activated PDMS block (left) and an AEAPTMS-treated PDMS block (right) bonded to an MPTMS-treated Au slide. Evidently, the AEAPTMS treatment on the PDMS enhances the bond strength as can be observed from the delamination of Au from the glass slide, whereas the standard O_2 plasma treatment did not result in delamination. We achieved higher assembly efficiencies with the PDMS functionalization protocol (yield > 95%) compared to the standard plasma activation protocol (yield < 15%). Once assembled (Figure 1B and 2F), we tested the devices for leaks and did not observe leaks even at high applied flow rates ($Q = 200 \mu\text{L}/\text{min}$). Furthermore, the device remained conductive (~ 10 ohms) during all assembly steps indicating a successful integration of the electrodes in the multilayer architecture.

Automated High-Throughput Analysis Workflow.

High-throughput workflows that require precise delivery of biomolecules for cellular manipulation applications or sensitive detection and quantification of intracellular molecules are possible with the LCAD. The reversible clamping between the device and conductive substrates (e.g., ITO slides with embedded surface-based sensors such as in SAMDI) enables for parallel analysis pipelines after electroporation, such as live-cell imaging and high-throughput mass spectrometry (Figure 1D). To accurately identify the cells in the culture wells, for subsequent analysis of their corresponding features (size, intensity, number of neighbors, texture), we employed a deep learning approach in which we trained a fully convolutional network (FCN)³⁴ with a U-Net³⁵ architecture containing 20 hidden layers to classify each pixel in the image into three categories: cell-interior, cell-boundary, or background. Segmenting the cells in this manner enabled the extraction of hundreds of morphological features using an image profiling

software (CellProfiler)³⁶ and correlation of extracted features with respect to other features, experimental inputs, or analytical measurements of extracted molecules. To obtain quantitative measurements of sampled enzymes, we measured the mass spectra of the SAMDI slides using a high-throughput MALDI-TOF instrument. We note that the platform is amenable to the detection of other molecule types by interfacing the LCAD with other surface-based assays, e.g., DNA-encoded antibody libraries (DEAL),³⁷ nanoplasmonic sensors,³⁸ or digital ELISA,³⁹ or by introduction of barcoded beads in the extraction chambers designed to capture mRNA transcripts.⁴⁰ A key advantage of the localized electroporation mechanism is its nondestructive nature, which allows for multiple stimulations and temporal measurements of sampled molecules from live-cells as demonstrated here and in our previous work.²⁶

Multitime Point Molecular Delivery. The localized electroporation mechanism allows for the precise delivery of molecules of various sizes into live cells while preserving viability. As a result, delivery of molecular cargoes into the same group of cells, at multiple time points, is possible with this system. To demonstrate such capability, we delivered EGFP plasmid (300 ng mL⁻¹) into HeLa cells immediately after cell-seeding and codelivered mCherry plasmid (300 ng mL⁻¹) with EGFP-siRNA (500 nM) 24 h later (Figure 3A). Fluorescence micrographs were taken with the automated imaging system at various time points (Figure 3B) following the first electroporation stimulation to track the expression of EGFP and mCherry protein in the cells. Evidently, cells started to express the EGFP protein shortly after delivery (1 h) with the number of EGFP-expressing cells increasing for up to 24 h. Following the codelivery of EGFP-siRNA and mCherry plasmid, the percentage of cells with EGFP expression at 48 h relative to the cells expressing EGFP at 24 h was significantly reduced (Figure 3C) indicating successful knockdown. Conversely, there was no statistically significant difference between the number of mCherry-expressing cells at 48 h relative to the number of EGFP-expressing cells at 24 h. Our results indicate that both cargoes were successfully delivered into the cells at the two time-points while maintaining the functionality of each delivered molecule. The ability to perform multiple deliveries sequentially is a capability of substrate-based electroporation systems.⁴¹ In contrast, other delivery systems are either too stressful on the cells (e.g., bulk-electroporation) to permit multiple stimulations or cannot be used to track the cells (e.g., bulk-electroporation or flow-based mechanoporation) during the experiments. Our microwell array design coupled with the AI-enhanced imaging pipeline enables the tracking of small populations of cells during the experiments with spatial accuracy, which is an advantage of the device compared to other substrate-based electroporation architectures. Delivery of functional molecules such as small siRNA or large plasmids, with dosage precision and temporal control, makes the LCAD a powerful tool for applications in systems biology, cellular engineering, and molecular biology.

To characterize the spatial uniformity of delivery in the LCAD array, we cultured Td-Tomato expressing breast cancer cells (MDA-MB 231) in the culture wells and delivered Alexa Fluor 488 (AF488)-tagged BSA protein (Figure 3 D,E). The spatial heatmap (Figure 3F) reveals row and column uniformity in delivery efficiency.

Enzyme Sampling and Device Characterization with SAMDI. The LCAD's ability to allow quantitative measure-

ments of extracted molecules from live cells provides a method to temporally interrogate the cells' internal state. Previously, we interfaced the LCAD with a SAMDI assay to measure enzyme activity temporally and in response to a perturbing agent.²⁶ Here, we interfaced the LCAD with a SAMDI slide, engineered to measure the activity of protein tyrosine phosphatases (PTP), to characterize the performance of sampling with different device designs and experimental inputs. To test the hypothesis that the addition of a conductive layer in the multilayer LCAD architecture enhances electroporation, we constructed two LCAD configurations, one with a gold layer and one without, and performed the electroporation protocol with a SAMDI slide attached to the PDMS reaction wells. Addition of the gold electrode increases the average measured PTP activity, compared to the device without gold and a control device where no electrical pulses were applied (Figure 4A). This result is consistent with the prediction of a lumped

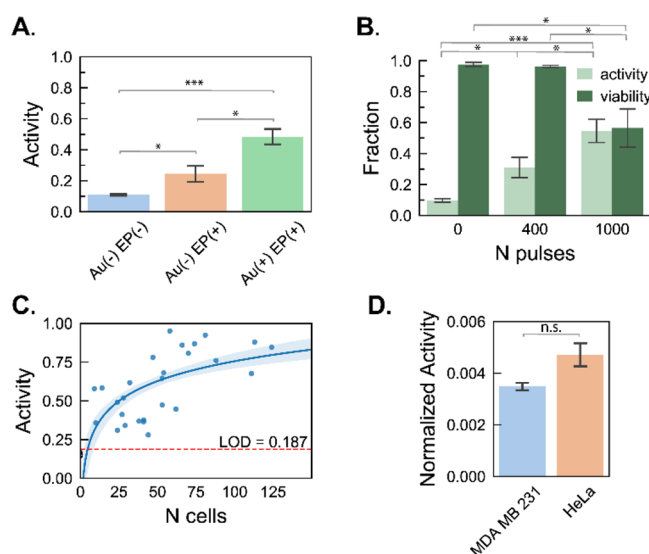


Figure 4. Enzyme sampling and detection with LCAD-SAMDI. (A) PTP enzyme activity of MDA-MB 231 cells sampled (EP+) with LCAD containing gold (Au+), without gold (Au-), and control device without electric stimulation (EP-) (standard error of mean bars, $N = 16$ wells/condition). (B) Bar plots of fractional PTP activity and viability with various pulse numbers. (C) Scatter plot of PTP activity with respect to number of cells. A horizontal dashed line is used to represent the limit of detection (LOD), which was calculated from control regions with zero cells. (D) Bar plot of PTP activity normalized with number of cells for MDA-MB 231 and HeLa cells. p -values used to determine statistical significance (n.s.: p -value > 0.05 , *: $0.01 < p$ -value < 0.05 , **: $0.001 < p$ -value < 0.01 , ***: p -value < 0.001).

model concerning increased TMP for LCAD configurations containing a conductive electrode layer. Furthermore, it is important to note that there is measurable activity above the limit of detection for the control device where no electric pulses were applied, which suggests that enzymes diffuse out of the cells during the incubation period in hypo-osmolar buffer with the SAMDI slide. Incubation with hypo-osmolar buffer leads to cell swelling, which enhances the electroporation performance due to increase in the membrane tension,¹⁸ but also could result in the formation of small pores and consequent leakage.^{2,42} However, we note that the measured activity for the control device is significantly less than the electroporated devices.

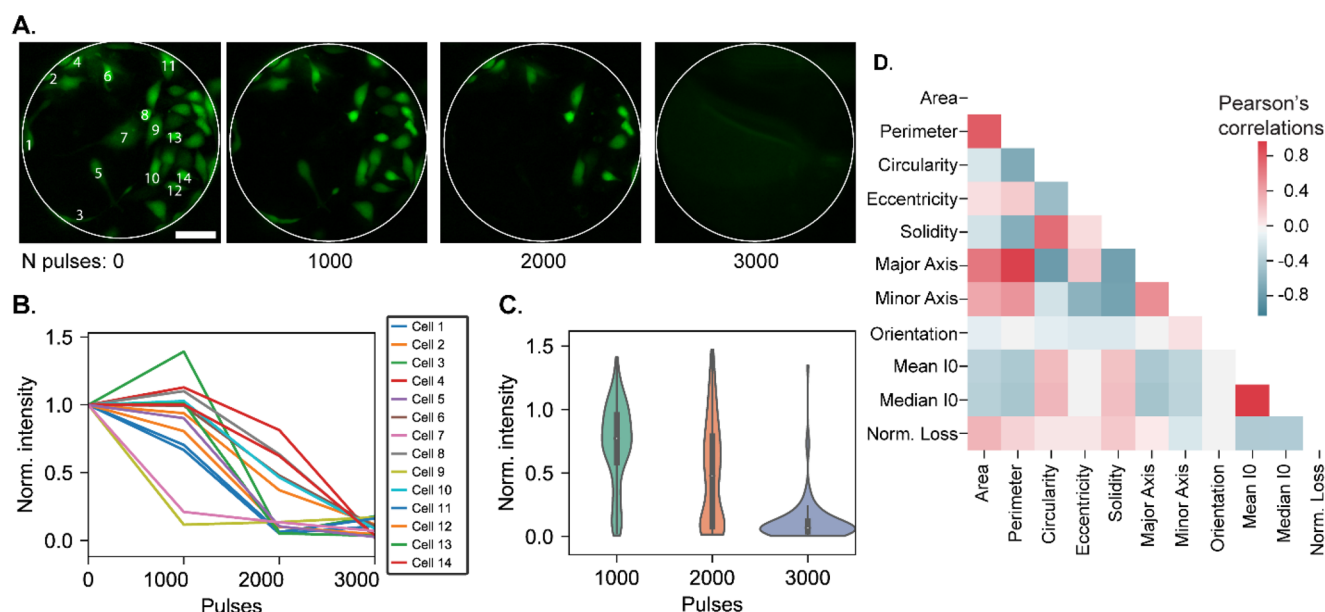


Figure 5. Dynamics of calcein sampling. (A) Fluorescent micrographs of MDA-MB231 cells stained with calcein AM (green) post electric pulse stimulations. Scale bar = 50 μm . (B) Line-plots of mean fluorescence intensity after multiple pulse applications corresponding to cells from (A). (C) Violin plots of the distribution of fluorescence intensity normalized with initial intensity after multiple pulse applications ($n_{\text{cells}} = 254$, $n_{\text{wells}} = 5$). (D) Pearson correlation heatmap of selected shape and intensity-based features obtained from single cells prior to electroporation ($N_{\text{pulse}} = 0$) and normalized calcein depletion (Norm. Loss) after 1000 pulses.

Electroporation-induced extraction of cytosolic molecules is believed to be diffusion dominant;^{27,43} therefore, molecular diffusivity, cellular localization, concentration, nanopore radius, and nanopore density are key factors that affect the quantity and identity of the sampled molecules. Consequently, sampling larger molecules may be challenging due to their low diffusivity and may not be possible if the hydrodynamic radius of the molecule is larger than the radius of the nanopores. Note that the radius of nanopores is dynamic,¹⁸ and in the case of reversible permeabilization the pores reseal over time, which limits the time for which molecules can diffuse across the cell membrane. Therefore, control over the amount of sampled content can be achieved by tuning the electroporation parameters (i.e., voltage, pulse duration, and number of pulses) to generate pores of sufficiently large size to sample the molecule of interest. Accordingly, we measured the activity of sampled cytosolic PTP, which ranges in size from (20–68 kDa), with different numbers of applied pulses (Figure 4B) and calculated viability of MDA-MB231 cells. The activity of sampled PTP increases with the number of pulses, which we hypothesize to be the result of longer poration times with increasing number of pulses. However, increasing the pulse number also resulted in a reduction of cell viability from 93% to 51%. The experiments revealed that in multitime-point sampling applications, the number of pulses must be limited to 400 pulses for the employed voltage conditions ($V = 30\text{ V}$, $f = 20\text{ Hz}$).

To test the sensitivity of the LCAD-SAMDI platform, we electroporated HeLa cells seeded in wells of different diameters to control the number of cells and measured PTP activity at each well. We successfully measured activity above the limits of detection from as few as nine cells (Figure 4C) and measured activity near saturation levels (i.e., activity = 1) in some wells from as few as ~ 60 cells. Measurements near saturation levels could be a result from the nearly complete cleavage of phosphate groups from the immobilized peptides on the SAM

by the extracted PTP enzymes. For applications that require sampling at multiple time points, however, it is advantageous to determine the dynamic range of the enzyme activity with the number of cells prior to the temporal sampling experiments to properly select the cell seeding density and incubation times necessary to obtain a measurable signal that does not approach saturation. Interestingly, PTP activity measurements obtained from wells with full confluency ($n_{\text{cells}} > 100$) did not result in activity measurements near saturation, which could be due to the cells having limited space to spread out and form a strong attachment to the nanochannel substrate. Additionally, a reduction in cortical tension could result from overcrowding, which may lead to less optimal electroporation conditions.⁴⁴ Such variabilities in the cell-culture conditions in addition to experimental factors, such as slight misalignment between the LCAD and SAMDI during clamping or air-bubble entrapment, may result in deviations of individual data points from the fitted curve, and therefore, quality control steps are necessary to reduce these effects. We predict that single cell resolutions may be achievable by reducing the extraction well volume and through further optimization of the electroporation parameters. Lastly, we calculated the activity of extracted PTP, normalized by the number of cells, for two cancer cell types (MDA-MB-231 and HeLa) and found no statistically significant difference (Figure 4D). It is known that PTP enzymes, and their protein kinase counterparts, are fundamental to the regulation of signal transduction pathways. Consequently, abnormal growth and proliferation in cancer cells has been linked to misregulation of these enzymes. The implication is that the high-throughput LCAD-SAMDI platform offers an experimental tool to test the effect of therapeutic drugs, such as PTP inhibitors⁴⁵ among others, in live cells.

Sampling Dynamics and Morphology Analysis. To test the rate of extraction of small molecules from adhered cells and to visualize the sampling process in the wells during electroporation, we seeded MDA-MB-231 cells in the culture

wells and stained them with a fluorescent dye (calcein AM) prior to electroporation. We applied electroporation pulses ($V = 30$ V, $f = 20$ Hz) and imaged the cells after successive trains of 1000 pulses (Figure 5A). A decrease in the mean fluorescence intensity, normalized with respect to the initial intensity (Figure 5B), indicates successful extraction of the calcein molecules from the cell cytosol. The distribution profile (Figure 5C) of the individual cells is bimodal after pulse applications up to 2000 pulses and reaches complete fluorescence depletion for the majority of cells after the application of 3000 pulses. The bimodal distribution of fluorescence loss indicates that one subpopulation of cells exhibits a small loss in fluorescence while another subpopulation exhibits a larger loss. Conversely, the well-to-well distribution of fluorescence depletion is unimodal, which indicates a similar sampling response across the device.

To examine whether the morphology of the cells contributes to the dynamics of calcein fluorescence loss, we extracted a variety of shape and intensity features from each cell using a deep-learning-based cell detection and feature extraction workflow. Next, we calculated the mean fluorescence intensity loss for each cell, after the first electroporation stimulation ($N_{\text{pulses}} = 1000$), and correlated it to the extracted features using a Pearson's correlation matrix (Figure 5D).⁴⁶ We observed that several shape features (including area, perimeter, and solidity) are positively correlated to the normalized fluorescence loss for each cell, whereas intensity features (i.e., mean initial intensity) are negatively correlated. Based on these results, we hypothesize that large and well-adhered cells are sampled at a higher rate compared to small rounded cells that also exhibit higher initial intensities. This is because large and well-adhered cells are in contact with a larger number of nanochannels and may have higher membrane tensions, which has been shown to increase electroporation performance.¹⁸ Therefore, to enhance sampling performance it is recommended to seed cells at low or medium densities to enable sufficient room for attachment and spreading within the microwells. We note that the deep-learning-enhanced image profiling proved to be a useful tool for temporal single-cell analysis and for ascertaining system performance. Moreover, the methodology is applicable to other studies such as the delivery of intracellular probes (e.g., molecular beacons¹⁹ and force-intercalation aptamers⁴⁷) and subsequent tracking of intracellular molecular abundance, or for studies involving the delivery of functional molecular cargoes, such as CRISPR-Cas9 complexes, and subsequent quantification of changes in cell morphology and proliferation.

CONCLUSION

We report the design and characterization of a versatile multilayer microfluidic platform consisting of microwell arrays for the active delivery and sampling of biomolecules in live cells. The modular design provides flexibility in experimental workflows for various manipulation and analysis tasks. Guided by a lumped model,¹⁸ a multilayer device design with embedded gold electrodes resulted in enhanced sampling and consistency in the electroporation conditions. Furthermore, the fabrication protocol presented here enabled the robust assembly of thin layers comprised of various materials, which can be extended to the fabrication of multilayer devices integrating 3D fluidic networks with metal electrodes.

By employing an automated imaging workflow, we demonstrated delivery of functional molecules (plasmid and

siRNA) at multiple-time-points and tracked their fluorescence expression *temporally*. Furthermore, we reported sampling performance enhancements, with well-to-well uniformity in measured enzyme activity while maintaining high cell viability, achieving saturation levels of protein tyrosine phosphatases activity measured from as few as 60 cells and demonstrated control over the amounts of sampled contents by optimization of electroporation parameters. We also revealed that cell morphology plays an important role in the efficiency of electroporation-induced sampling, which suggest directions for future research to improve sampling performance. The capability to nondestructively extract cytosolic contents with consistency is essential to interrogate the intracellular state of cells in a quantitative manner. In this context, the various capabilities of the LCAD device here reported provide a powerful path for the temporal analysis and perturbation of live cells in a scalable microarray format. We must note, however, that sampling from a single cell remains a challenging task primarily due to the small quantities of analytes extracted. With further improvements in electroporation protocols, to sample greater quantities of cytosolic material, and sensitivity of molecular assays, it may be possible to overcome this limitation. Moreover, in the future it may be possible to integrate the LCAD with barcoded beads for polyadenylated mRNA capture and next generation sequencing (NGS) to perform omics scale analysis on the sampled contents.

METHODS

Device Fabrication and Assembly. Molds were fabricated with positive photoresist material (SU8-2050, Microchem) to yield 50 μm tall features using photolithography equipment. Next, the molds were coated with a thin (~ 100 nm) layer of parylene C to lower the surface friction of the mold to facilitate the removal of PDMS from the mold. To prepare the PDMS, a mixture of elastomer and curing agent (10:1) was mixed and degassed in a desiccator for 45 min. To fabricate the microchannel layer, the PDMS mixture was poured on the microchannel mold and placed in a convection oven at 80 $^{\circ}\text{C}$ for 2 h. The through-hole microwell stencil layers were fabricated by selectively polymerizing the PDMS by application of chelating aminosilanes on a flexible transfer sheet as described in the reference.³⁰ A flexible electrode layer was aggregated to the surface of the PDMS stencil by sputter-coating a 10 nm Ti adhesion layer and a 100 nm Au layer while maintaining the substrate temperature at 80 $^{\circ}\text{C}$.

To bond the Au-coated PDMS culture wells to the PDMS microfluidic channel layers, the Au surface was functionalized with 25 mM mercaptopropyltrimethoxysilane (MPTMS, Sigma-Aldrich) in ethanol overnight. Next, the PDMS surface was functionalized with a double-amine silane, 1% (v/v) solution of aminoethylaminopropyltrimethoxysilane (AEAPTMS, Sigma-Aldrich) in DI water for 15 min before bonding to the MPTMS-coated Au surface at high temperature in a convection oven ($T = 110$ $^{\circ}\text{C}$) for 2 h.

To bond the PC nanochannel membrane between the two PDMS stencil layers (culture wells and reaction-wells) we functionalized the surfaces of the two PDMS layers with 1% (v/v) AEAPTMS in DI water for 20 min prior to bonding to an oxygen plasma activated PC nanochannel membrane at high temperature ($T = 110$ $^{\circ}\text{C}$) for 2 h. After assembly, the conductivity of the devices was measured with a multimeter and tested for leaks by introducing DI water at a flow rate of 100 $\mu\text{L}/\text{min}$.

Cell Seeding and On-Chip Cell Culture. Prior to seeding, devices were cleaned in UV for 24 h, rinsed with DI water and ethanol, and coated with fibronectin solution in PBS (0.4% v/v) for 2 h. Following surface treatment, the fibronectin solution was rinsed with PBS for 10 min. Cells were removed from the cell-culture flasks (T-35, Falcon) by adding 1 mL of 0.25% trypsin-EDTA (Gibco), suspended to a density of 1×10^6 (cells/mL), and introduced into the

LCAD using a programmable syringe pump. Fresh media was perfused in the channels every 12 h for 10 min for experiments requiring long-term culture.

Electroporation Protocol. To prepare the cells for electroporation, electroporation buffer (Eppendorf) was introduced into the device for 10 min. For molecular delivery experiments, the device was sandwiched between two ITO slides, clamped, and connected to a programmable function generator. For sampling and quantitative detection experiments, the devices were sandwiched between an ITO slide (top) and a SAMDI substrate (bottom) and connected to a programmable function generator. The following voltage parameters were set prior to electrical stimulation: voltage amplitude, pulse duration, pulse-shape, number of pulses, and frequency. To enhance electrophoretic induced transport a bilevel pulse profile was utilized for all experiments.

SAMDI Mass Spectrometry. A SAMDI sensor was prepared on steel plates or transparent ITO slides (Nanocs) to enable facile alignment by depositing a 5 nm Ti adhesion layer and a 30 nm Au layer through an aluminum mask containing the reaction-well features with additional control features. An ethanolic solution containing alkyl disulfide terminated with tri(ethylene glycol) groups (0.4 mM) and asymmetric disulfide terminated with one tri(ethylene glycol) and one maleimide group (0.1 mM) was prepared. The ITO-Au slides were placed in the solution at 4 °C overnight to form a monolayer on the Au features. To functionalize the monolayer surface for specific detection of PTP, a peptide containing phosphotyrosine, CRpY-NH₂ (40 μM), in Tris buffer (25 mM, pH = 8) was immobilized for 1 h in an incubator (37 °C). After the immobilization step concluded, the functionalized SAMDI slide was rinsed with DI water and ethanol and dried prior to alignment and clamping with the PDMS reaction-wells.

To sample PTP, the clamped SAMDI-LCAD assembly was placed in an incubator (37 °C, 5% CO₂) for 1 h following the electroporation protocol. Next, the SAMDI slide was detached from the LCAD and rinsed with water and ethanol. To prepare the SAMDI slide for mass spectrometry, the SAMDI slide was coated with a solution of 2,4,6-trihydroxyacetophenone in acetone (40 mg/mL) and subsequently dried. The SAMDI slide was then inserted in a high-throughput MALDI-TOF instrument (AB Sciex) to measure the mass properties of the slide. The enzymatic activity was calculated from obtaining the area under the curve (AUC) of the product and substrate peaks [$\text{product}/(\text{product} + \text{substrate})$]_{AUC}.

Automated Imaging, AI Detection, And Analysis. The imaging setup consisted of an inverted microscope (Nikon Ti-E) equipped with a motorized stage, fluorescent filter cubes, and a CCD camera (Andor Neo). A custom Python script was programmed to control the motorized stage movement in order to automatically acquire images of each well in the LCAD array.

A fully convolutional network³⁴ consisting of a U-Net encoder-decoder architecture containing 20 hidden layers was utilized to segment and identify the cells in each image. The U-Net was trained to detect the cells in our studies using automatically acquired ground truth labels as described in our previous work.⁴⁸ The trained U-Net models were optimized for inference acceleration (Intel OpenVINO) to automatically detect the cells in each field of view following image acquisition.

The raw images and their corresponding labels obtained from the U-Net detection were passed through a feature extraction pipeline (CellProfiler)³⁶ which measures hundreds of features of various categories (shape, intensity, texture, and microenvironment) for each cell. Following feature extraction, each feature was log transformed⁴⁹ and normalized using the robust Z-score (R.Z.score), which was calculated from the median and median absolute deviation using the following equation: $\text{R.Z.score} = \frac{X - \text{median}_X}{1.4826 \times \text{MAD}_X}$. Following normalization, the number of features was reduced by calculating the Pearson correlation of each feature pair and iteratively removing features exceeding a certain threshold ($r^2 > 0.9$).

Cell Viability. To measure viability, a live/dead assay solution with (1 μg/mL) calcein AM (Sigma-Aldrich) live marker and (0.1 mg/mL) Hoechst (Life Technologies) nuclear marker was prepared

in PBS, introduced to the LCAD channels for 10 min, and subsequently rinsed with PBS for 10 min. The automated imaging and analysis pipeline was utilized to automatically count the number of live cells (Calcein AM) and the total number of cells (Hoechst) in each well to calculate viability.

CFD Modeling. The CFD model was implemented using commercial software (ANSYS Fluent). A uniform grid mesh constructed from 1 μm² elements was used and defined one velocity inlet and four pressure outlets (three located at the bottom microwells and one at the exit of microfluidic channel). A porous zone module was used to model the nanochannel membrane. The fluid velocity and pressure was calculated using the Semi-Implicit Method for Pressure-Linked Equations (SIMPLE)⁵⁰ algorithm. A Power Law scheme was used to solve for the advection-diffusion equations using under-relaxation factors (β : $\beta_{\text{pressure}} = 0.2$ and $\beta_{\text{velocity}} = 0.6$) to achieve convergence. A time-step-size of 0.005 s was used for a total of 0.5 s. The discrete phase modeling (DPM) module was used to simulate the trajectory of the cell in the device with two flow rates (0.4 μL/min and 1 μL/min). The fluid flow velocity was initialized to a steady state flow prior to particle injection with the following injection parameters: particle diameter ($D_{\text{particle}} = 5 \mu\text{m}$), particle density ($\rho_{\text{particle}} = 1080 \text{ kg/m}^3$), inject velocity ($v_{\text{inject}} = 0 \text{ m/s}$), and injection position ($X_{\text{inject}} = \text{inlet center}$).

Statistical Analysis. Statistical analysis operations were performed with a custom Python script. A Pearson correlation matrix was used to compute the correlation of extracted features. To determine the statistical significance between two conditions, a two-tailed Student's *t* test was used. A two-way ANOVA analysis was utilized to measure statistical variations along the rows and columns of the devices to quantify device uniformity. For SAMDI measurements, the limits of detection (LOD) for each experiment was calculated from control spots aligned to LCAD regions containing zero cells as follows: $\text{LOD} = \mu + 3\sigma$, where μ is the mean activity and σ is the standard deviation of the activity of the control spots.

ASSOCIATED CONTENT

Supporting Information

The Supporting Information is available free of charge at <https://pubs.acs.org/doi/10.1021/acsnano.2c00698>.

Results of CFD modeling and cell seeding in the LCAD microfluidic device; detailed explanation of lumped model analysis, used to calculate the transmembrane potential of cells in LCAD, includes list of parameters, equations, and results (PDF)

AUTHOR INFORMATION

Corresponding Author

Horacio D. Espinosa – Department of Mechanical Engineering, Northwestern University, Evanston, Illinois 60208, United States; Theoretical and Applied Mechanics Program and Department of Biomedical Engineering, Northwestern University, Evanston, Illinois 60208, United States; orcid.org/0000-0002-1907-3213; Email: espinosa@northwestern.edu

Authors

Cesar A. Patino – Department of Mechanical Engineering, Northwestern University, Evanston, Illinois 60208, United States; orcid.org/0000-0003-3074-9314

Prithvijit Mukherjee – Department of Mechanical Engineering, Northwestern University, Evanston, Illinois 60208, United States; Theoretical and Applied Mechanics Program, Northwestern University, Evanston, Illinois 60208, United States

Eric J. Berns – Department of Biomedical Engineering, Northwestern University, Evanston, Illinois 60208, United States; orcid.org/0000-0002-2203-0847

Elamar Hakim Mouly – Department of Chemistry, Northwestern University, Evanston, Illinois 60208, United States

Liliana Stan – Center for Nanoscale Materials, Argonne National Laboratory, Argonne, Illinois 60439, United States

Milan Mrksich – Department of Biomedical Engineering and Department of Chemistry, Northwestern University, Evanston, Illinois 60208, United States; Department of Cell & Developmental Biology, Northwestern University, Chicago, Illinois 60611, United States; orcid.org/0000-0002-4964-796X

Complete contact information is available at:
<https://pubs.acs.org/10.1021/acsnano.2c00698>

Author Contributions

H.D.E. and M.M. conceived the project. C.A.P., P.M., and E.J.B. designed the devices. C.A.P. and L.S. fabricated the devices. C.A.P., P.M., E.J.B., and E.H.M. performed the experiments. C.A.P. developed the AI-imaging pipeline. All authors analyzed and interpreted the data. C.A.P., E.J.B., P.M., M.M., and H.D.E. wrote the manuscript.

Notes

The authors declare the following competing financial interest(s): H.D.E. is the founder and majority owner of Infinitesimal LLC, a company commercializing bio-tools for gene editing and cell analysis. M.M. is the founder of SAMDI Tech Inc., which uses SAMDI-MS to assist clients in the pharmaceutical industry.

ACKNOWLEDGMENTS

Research reported in this publication was supported by the National Cancer Institute of the National Institutes of Health (NIH) under Award No. U54CA199091 and by NIH R21 Award No. GM132709-01. This work utilized the Argonne National Lab Center for Nanoscale Materials. Work performed at the Center for Nanoscale Materials, a U.S. Department of Energy Office of Science User Facility, was supported by the U.S. DOE, Office of Basic Energy Sciences, under Contract No. DE-AC02-06CH11357. Cells were obtained from the Northwestern University Developmental Therapeutics Core generously supported by NCI CCSG P30 CA060553 awarded to the Robert H Lurie Comprehensive Cancer Center. This work made use of the NUFAB facility of Northwestern University's NUANCE Center, which has received support from the SHyNE Resource (NSF ECCS-2025633), the IIN, and Northwestern's MRSEC program (NSF DMR-1720139).

REFERENCES

- (1) Prakadan, S. M.; Shalek, A. K.; Weitz, D. A. Scaling by Shrinking: Empowering Single-Cell 'Omics' with Microfluidic Devices. *Nat. Rev. Genet.* **2017**, *18* (6), 345–361.
- (2) Stewart, M. P.; Sharei, A.; Ding, X.; Sahay, G.; Langer, R.; Jensen, K. F. In Vitro and Ex Vivo Strategies for Intracellular Delivery. *Nature* **2016**, *538* (7624), 183–192.
- (3) Qin, W.; Dion, S. L.; Kutny, P. M.; Zhang, Y.; Cheng, A. W.; Jillette, N. L.; Malhotra, A.; Geurts, A. M.; Chen, Y.-G.; Wang, H. Efficient Cas9/Cas9-Mediated Genome Editing in Mice by Zygote Electroporation of Nuclease. *Genetics* **2015**, *200* (2), 423–430.
- (4) Yang, R.; Lemaitre, V.; Huang, C.; Haddadi, A.; McNaughton, R.; Espinosa, H. D. Monoclonal Cell Line Generation and Cas9 Manipulation Via Single-Cell Electroporation. *Small* **2018**, *14* (12), 1702495.

- (5) Espinosa, H. D.; Mukherjee, P.; Patino, C. Nanofountain Probe Electroporation for Monoclonal Cell Line Generation. In *Electroporation Protocols: Microorganism, Mammalian System, and Nanodevice*; Li, S., Chang, L., Teissie, J., Eds.; Springer US: New York, 2020; pp 59–68.
- (6) Balboa, D.; Weltner, J.; Euroola, S.; Trokovic, R.; Wartiovaara, K.; Otonkoski, T. Conditionally Stabilized Dcas9 Activator for Controlling Gene Expression in Human Cell Reprogramming and Differentiation. *Stem Cell Rep* **2015**, *5* (3), 448–459.
- (7) Neumann, E.; Schaefer-Ridder, M.; Wang, Y.; Hofschneider, P. Gene Transfer into Mouse Lyoma Cells by Electroporation in High Electric Fields. *EMBO J.* **1982**, *1* (7), 841–845.
- (8) Gehl, J. Electroporation: Theory and Methods, Perspectives for Drug Delivery, Gene Therapy and Research. *Acta. Physiol. Scand.* **2003**, *177* (4), 437–447.
- (9) Sharei, A.; Zoldan, J.; Adamo, A.; Sim, W. Y.; Cho, N.; Jackson, E.; Mao, S.; Schneider, S.; Han, M.-J.; Lytton-Jean, A.; et al. A Vector-Free Microfluidic Platform for Intracellular Delivery. *Proc. Natl. Acad. Sci. U.S.A.* **2013**, *110* (6), 2082–2087.
- (10) Adamo, A.; Jensen, K. F. Microfluidic Based Single Cell Microinjection. *Lab Chip* **2008**, *8* (8), 1258–1261.
- (11) Dixit, H. G.; Starr, R.; Dundon, M. L.; Pairs, P. I.; Yang, X.; Zhang, Y.; Nampe, D.; Ballas, C. B.; Tsutsui, H.; Forman, S. J.; et al. Massively-Parallelized, Deterministic Mechanoporation for Intracellular Delivery. *Nano Lett.* **2020**, *20* (2), 860–867.
- (12) Loh, O. Y.; Ho, A. M.; Rim, J. E.; Kohli, P.; Patankar, N. A.; Espinosa, H. D. Electric Field-Induced Direct Delivery of Proteins by a Nanofountain Probe. *Proc. Natl. Acad. Sci. U.S.A.* **2008**, *105* (43), 16438–16443.
- (13) Cao, Y.; Chen, H.; Qiu, R.; Hanna, M.; Ma, E.; Hjort, M.; Zhang, A.; Lewis, R. S.; Wu, J. C.; Melosh, N. A. Universal Intracellular Biomolecule Delivery with Precise Dosage Control. *Sci. Adv.* **2018**, *4* (10), No. eaat8131.
- (14) Boukany, P. E.; Morss, A.; Liao, W. C.; Henslee, B.; Jung, H. C.; Zhang, X. L.; Yu, B.; Wang, X. M.; Wu, Y.; Li, L.; et al. Nanochannel Electroporation Delivers Precise Amounts of Biomolecules into Living Cells. *Nat. Nanotechnol.* **2011**, *6* (11), 747–754.
- (15) Kang, W.; Giraldo-Vela, J. P.; Nathamgari, S. S. P.; McGuire, T.; McNaughton, R. L.; Kessler, J. A.; Espinosa, H. D. Microfluidic Device for Stem Cell Differentiation and Localized Electroporation of Postmitotic Neurons. *Lab Chip* **2014**, *14* (23), 4486–4495.
- (16) Kang, W.; Yavari, F.; Minary-Jolandan, M.; Giraldo-Vela, J. P.; Safi, A.; McNaughton, R. L.; Parpoil, V.; Espinosa, H. D. Nanofountain Probe Electroporation (Nfp-E) of Single Cells. *Nano Lett.* **2013**, *13* (6), 2448–2457.
- (17) Kang, W.; McNaughton, R. L.; Espinosa, H. D. Micro- and Nanoscale Technologies for Delivery into Adherent Cells. *Trends Biotechnol.* **2016**, *34* (8), 665–678.
- (18) Mukherjee, P.; Nathamgari, S. S. P.; Kessler, J. A.; Espinosa, H. D. Combined Numerical and Experimental Investigation of Localized Electroporation-Based Cell Transfection and Sampling. *ACS Nano* **2018**, *12* (12), 12118–12128.
- (19) Giraldo-Vela, J. P.; Kang, W.; McNaughton, R. L.; Zhang, X. M.; Wile, B. M.; Tsourkas, A.; Bao, G.; Espinosa, H. D. Single-Cell Detection of mRNA Expression Using Nanofountain-Probe Electroporated Molecular Beacons. *Small* **2015**, *11* (20), 2386–2391.
- (20) Cao, Y.; Ma, E.; Cestellos-Blanco, S.; Zhang, B.; Qiu, R.; Su, Y.; Doudna, J. A.; Yang, P. Nontoxic Nanopore Electroporation for Effective Intracellular Delivery of Biological Macromolecules. *Proc. Natl. Acad. Sci. U.S.A.* **2019**, *116* (16), 7899–7904.
- (21) Mukherjee, P.; Patino, C. A.; Pathak, N.; Lemaitre, V.; Espinosa, H. D. Deep Learning-Assisted Automated Single Cell Electroporation Platform for Effective Genetic Manipulation of Hard-to-Transfect Cells. *Small* **2022**, 2107795.
- (22) Higgins, S. G.; Stevens, M. M. Extracting the Contents of Living Cells. *Science* **2017**, *356* (6336), 379–380.

- (23) Actis, P.; Maalouf, M. M.; Kim, H. J.; Lohith, A.; Vilozny, B.; Seger, R. A.; Pourmand, N. Compartmental Genomics in Living Cells Revealed by Single-Cell Nanobiopsy. *ACS Nano* **2014**, *8* (1), 546–553.
- (24) Nadappuram, B. P.; Cadinu, P.; Barik, A.; Ainscough, A. J.; Devine, M. J.; Kang, M.; Gonzalez-Garcia, J.; Kittler, J. T.; Willison, K. R.; Vilar, R.; et al. Nanoscale Tweezers for Single-Cell Biopsies. *Nat. Nanotechnol.* **2019**, *14* (1), 80–88.
- (25) Guillaume-Gentil, O.; Grindberg, R. V.; Kooger, R.; Dorwling-Carter, L.; Martinez, V.; Ossola, D.; Pilhofer, M.; Zambelli, T.; Vorholt, J. A. Tunable Single-Cell Extraction for Molecular Analyses. *Cell* **2016**, *166* (2), 506–516.
- (26) Mukherjee, P.; Berns, E. J.; Patino, C. A.; Hakim Mouly, E.; Chang, L.; Nathangari, S. S. P.; Kessler, J. A.; Mrksich, M.; Espinosa, H. D. Temporal Sampling of Enzymes from Live Cells by Localized Electroporation and Quantification of Activity by Sandi Mass Spectrometry. *Small* **2020**, *16* (26), 2000584.
- (27) Cao, Y.; Hjort, M.; Chen, H.; Birey, F.; Leal-Ortiz, S. A.; Han, C. M.; Santiago, J. G.; Paşca, S. P.; Wu, J. C.; Melosh, N. A. Nondestructive Nanostraw Intracellular Sampling for Longitudinal Cell Monitoring. *Proc. Natl. Acad. Sci. U.S.A.* **2017**, *114* (10), E1866–E1874.
- (28) Caicedo, J. C.; Goodman, A.; Karhohs, K. W.; Cimini, B. A.; Ackerman, J.; Haghighi, M.; Heng, C.; Becker, T.; Doan, M.; McQuinn, C. Nucleus Segmentation across Imaging Experiments: The 2018 Data Science Bowl. *Nat. Methods* **2019**, *16* (12), 1247–1253.
- (29) Mrksich, M. Mass Spectrometry of Self-Assembled Monolayers: A New Tool for Molecular Surface Science. *ACS Nano* **2008**, *2* (1), 7–18.
- (30) Karlsson, J. M.; Haraldsson, T.; Carlborg, C. F.; Hansson, J.; Russom, A.; van der Wijngaart, W. Fabrication and Transfer of Fragile 3d Pdms Microstructures. *J. Micromech. Microeng.* **2012**, *22* (8), 085009.
- (31) Bowden, N.; Brittain, S.; Evans, A. G.; Hutchinson, J. W.; Whitesides, G. M. Spontaneous Formation of Ordered Structures in Thin Films of Metals Supported on an Elastomeric Polymer. *Nature* **1998**, *393* (6681), 146–149.
- (32) Choi, W. M.; Song, J.; Khang, D.-Y.; Jiang, H.; Huang, Y. Y.; Rogers, J. A. Biaxially Stretchable “Wavy” Silicon Nanomembranes. *Nano Lett.* **2007**, *7* (6), 1655–1663.
- (33) Lacour, S. P.; Wagner, S.; Huang, Z.; Suo, Z. Stretchable Gold Conductors on Elastomeric Substrates. *Appl. Phys. Lett.* **2003**, *82* (15), 2404–2406.
- (34) Long, J.; Shelhamer, E.; Darrell, T. Fully Convolutional Networks for Semantic Segmentation. In *Proceedings of the IEEE Conference on Computer Vision and Pattern Recognition (CVPR)*, Boston, MA, Jun 7–12, 2015; IEEE: New York, NY, 2015; pp 3431–3440.
- (35) Falk, T.; Mai, D.; Bensch, R.; Çiçek, Ö.; Abdulkadir, A.; Marrakchi, Y.; Böhm, A.; Deubner, J.; Jäkel, Z.; Seiwald, K. U-Net: Deep Learning for Cell Counting, Detection, and Morphometry. *Nat. Methods* **2019**, *16* (1), 67–70.
- (36) Carpenter, A. E.; Jones, T. R.; Lamprecht, M. R.; Clarke, C.; Kang, I. H.; Friman, O.; Guertin, D. A.; Chang, J. H.; Lindquist, R. A.; Moffat, J. Cellprofiler: Image Analysis Software for Identifying and Quantifying Cell Phenotypes. *Genome Biol.* **2006**, *7* (10), 1–11.
- (37) Bailey, R. C.; Kwong, G. A.; Radu, C. G.; Witte, O. N.; Heath, J. R. DNA-Encoded Antibody Libraries: A Unified Platform for Multiplexed Cell Sorting and Detection of Genes and Proteins. *J. Am. Chem. Soc.* **2007**, *129* (7), 1959–1967.
- (38) Raphael, M. P.; Christodoulides, J. A.; Mulvaney, S. P.; Miller, M. M.; Long, J. P.; Byers, J. M. A New Methodology for Quantitative Lspr Biosensing and Imaging. *Anal. Chem.* **2012**, *84* (3), 1367–1373.
- (39) Rissin, D. M.; Kan, C. W.; Campbell, T. G.; Howes, S. C.; Fournier, D. R.; Song, L.; Piech, T.; Patel, P. P.; Chang, L.; Rivnak, A. J.; et al. Single-Molecule Enzyme-Linked Immunosorbent Assay Detects Serum Proteins at Subfemtomolar Concentrations. *Nat. Biotechnol.* **2010**, *28* (6), 595–599.
- (40) Macosko, E. Z.; Basu, A.; Satija, R.; Nemesh, J.; Shekhar, K.; Goldman, M.; Tirosh, I.; Bialas, A. R.; Kamitaki, N.; Martersteck, E. M. Highly Parallel Genome-Wide Expression Profiling of Individual Cells Using Nanoliter Droplets. *Cell* **2015**, *161* (5), 1202–1214.
- (41) Xie, X.; Xu, A. M.; Leal-Ortiz, S.; Cao, Y.; Garner, C. C.; Melosh, N. A. Nanostraw–Electroporation System for Highly Efficient Intracellular Delivery and Transfection. *ACS Nano* **2013**, *7* (5), 4351–4358.
- (42) Groulx, N.; Boudreault, F.; Orlov, S. N.; Grygorczyk, R. Membrane Reserves and Hypotonic Cell Swelling. *J. Membr. Biol.* **2006**, *214* (1), 43–56.
- (43) Nathangari, S. S. P.; Pathak, N.; Lemaitre, V.; Mukherjee, P.; Muldoon, J. J.; Peng, C. Y.; McGuire, T.; Leonard, J. N.; Kessler, J. A.; Espinosa, H. D. Nanofountain Probe Electroporation Enables Versatile Single-Cell Intracellular Delivery and Investigation of Postpulse Electropore Dynamics. *Small* **2020**, *16* (43), 2002616.
- (44) Miroshnikova, Y. A.; Le, H. Q.; Schneider, D.; Thalheim, T.; Rübsam, M.; Bremicker, N.; Polleux, J.; Kamprad, N.; Tarantola, M.; Wang, I. Adhesion Forces and Cortical Tension Couple Cell Proliferation and Differentiation to Drive Epidermal Stratification. *Nat. Cell Biol.* **2018**, *20* (1), 69–80.
- (45) Heneberg, P. Use of Protein Tyrosine Phosphatase Inhibitors as Promising Targeted Therapeutic Drugs. *Curr. Med. Chem.* **2009**, *16* (6), 706–733.
- (46) Caicedo, J. C.; Cooper, S.; Heigwer, F.; Warchal, S.; Qiu, P.; Molnar, C.; Vasilevich, A. S.; Barry, J. D.; Bansal, H. S.; Kraus, O.; et al. Data-Analysis Strategies for Image-Based Cell Profiling. *Nat. Methods* **2017**, *14* (9), 849–863.
- (47) Ebrahimi, S. B.; Samanta, D.; Cheng, H. F.; Nathan, L. I.; Mirkin, C. A. Forced Intercalation (Fit)-Aptamers. *J. Am. Chem. Soc.* **2019**, *141* (35), 13744–13748.
- (48) Patino, C. A.; Mukherjee, P.; Lemaitre, V.; Pathak, N.; Espinosa, H. D. Deep Learning and Computer Vision Strategies for Automated Gene Editing with a Single-Cell Electroporation Platform. *SLAS Technol.* **2021**, *26* (1), 26–36.
- (49) Huber, W.; Von Heydebreck, A.; Sülthmann, H.; Poustka, A.; Vingron, M. Variance Stabilization Applied to Microarray Data Calibration and to the Quantification of Differential Expression. *Bioinformatics* **2002**, *18* (Suppl 1), S96–104.
- (50) Patankar, S. V. *Numerical Heat Transfer and Fluid Flow*; Hemisphere: Washington, D.C., 1980.